Interferometric Assessment of SAOCOM-1 TOPSAR Data

Jorge A. Euillades[ID], Yenni L. Roa, Leonardo D. Euillades[ID], Pablo A. Euillades, Patricia A. Rosell[ID], Edinson A. Solarte, and Stefano Perna[ID], *Senior Member, IEEE*

Abstract— Satélite Argentino de Observación COn Microondas (SAOCOM-1) constellation operates in three acquisition modes: Stripmap (SM), Terrain Observation with Progressive Scans Synthetic Aperture Radar (TOPSAR) Narrow (TNA and TNB), and TOPSAR Wide (TW). Since repeat-pass SAOCOM-1 TOPSAR acquisitions are not synchronized, the generation of the related interferometric products is not guaranteed, as it happens instead for the synchronized repeat-pass TOPSAR acquisitions, such as those of Sentinel-1. In this work, we assess the suitability of SAOCOM-1 TOPSAR acquisitions for generating interferometric products. To this aim, we first discuss the constraints that must be fulfilled by the repeat-pass nonsynchronized TOPS acquisitions in order to make it feasible the generation of usable interferograms. Then, we verify whether SAOCOM-1 TOPSAR acquisitions fulfill these constraints. For this purpose, we present an analysis based on the use of a dataset composed by 18 TNB images relevant to a single subswath illuminating a region located in the southwest of Argentina. From this dataset, we were able to select 48 pairs that guarantee the spectral superposition needed for interferometric purposes. We verified that 50% of these 48 pairs fulfill the constraint required to avoid in the corresponding interferograms the presence of noncoherent azimuth stripes, whose azimuth extension depends on one side on the mis-synchronization percentage between the repeat-pass acquisitions and the other side on the overlapping percentage between adjacent bursts of the same acquisition. Summing up, the presented analysis proves the potential of SAOCOM-1 TOPSAR acquisitions to obtain interferometric products, despite the absence of bursts synchronization between repeat-pass acquisitions.

Index Terms— Bursts synchronization, differential interferometry synthetic aperture radar (DInSAR), Satélite Argentino de Observación COn Microondas (SAOCOM-1), Terrain Observation with Progressive Scans SAR (TOPSAR).

I. INTRODUCTION

SATÉLITE Argentino de Observación COn Microondas (SAOCOM-1) is a spaceborne constellation developed by CONAE (Space Agency of Argentina), composed of two full-polarimetric synthetic aperture radar (SAR) (A and B) operating at a carrier frequency of 1.275 GHz (L-band). Both sensors operate in three acquisition modes: Stripmap (SM) [1], Terrain Observation with Progressive Scans SAR (TOPSAR) Narrow (TN), and TOPSAR Wide (TW) [2], which differ in coverage and spatial resolution [3]. Data can be acquired in single/dual and quad polarizations.

Mission scope is mainly the generation of soil moisture maps to support agriculture in the wide Pampas Region of Argentina, profiting from the regional scale of the TOPSAR data. Consequently, a large amount of information acquired in TOPSAR mode is usually available [4]. On the other side, SAR interferometry (InSAR) has not been defined in the specifications of the SAOCOM-1 mission for TOPSAR acquisitions, which are thus planned without burst synchronization. This means that in repeat-pass acquisitions, the radar is not constrained to observe a generic target on the ground always with the same squint angle, that is, with the same Doppler centroid (DC) [1]. Therefore, an adequate spectral overlap between repeat-pass bursts relevant to the same area on the ground is not guaranteed. For this reason, the interferometric processing of SAOCOM-1 TOPSAR data is a challenging, sometimes unfeasible, task, generally more complex than that of SAOCOM-1 SM [5], [6], [7] data or that of synchronized TOPSAR data [8], [9], [10], [11]. Within this context, evaluating the InSAR capabilities of SAOCOM-1 TOPSAR modes is of great interest, especially if we consider the great amount of available data acquired with these modes. In this work, we evaluate the suitability of SAOCOM-1 TOPSAR acquisitions for generating interferometric products.

To this aim, we first discuss the constraints that must be fulfilled by the repeat-pass nonsynchronized TOPS acquisitions in order to make it feasible the generation of usable interferograms (Section II). To do this, we introduce a metric to measure the mis-synchronization between repeat-pass bursts. Then, we show that depending on the amount of such mis-synchronization, two effects occur in the corresponding interferograms: coherence degradation and possible presence of totally incoherent azimuth stripes. Both effects are properly discussed and quantified in Sections II-A and II-B, respectively.

In Section III, we then verify whether SAOCOM-1 TOPSAR acquisitions fulfill the constraints discussed in Section II.

To this aim, we present an analysis based on the use of a dataset composed by 18 TNB images relevant to a single subswath illuminating a region located in the southwest of Argentina.

Concluding remarks are reported in Section IV.

II. NONSYNCHRONIZED TOPSAR: EFFECTS ON THE INTERFEROGRAMS

Let start from the TOPS mode acquisition geometry [2], and consider the scene interburst time period T and the corresponding number of azimuth lines X, which can be expressed as

$$X = T\,\mathrm{prf} \tag{1}$$

wherein prf is the pulse repetition frequency. Note that the burst duration is approximately equal to T/N_S, with N_S being the number of subswaths of the considered acquisition burst mode. Moreover, the azimuth extension of the ground region relevant to each burst, say X_g, can be expressed as $X_g = \alpha X$, where the factor $\alpha \geq 1$ accounts for the possible overlapping between adjacent bursts of the same acquisition. For the sake of simplicity, in the following, we will neglect the range dependence of α.

Turning to the repeat-pass scenario, let us consider two repeat-pass acquisitions that we name *reference* and *secondary*. Let consider two bursts, one for each acquisition, which include a generic illuminated target p. In the following, these two bursts are referred to as matching bursts. Let x_p^{ref} and x_p^{sec} be the azimuth lines corresponding to the target p in the two matching bursts. Let us define δx_p as the shift between them and Δx_p as its counterpart normalized to X

$$\Delta x_p = \frac{|x_p^{\mathrm{ref}} - x_p^{\mathrm{sec}}|}{X} = \frac{\delta x_p}{X}. \tag{2}$$

Note that Δx_p, which in the following is named as synchronization index, varies between 0, in the case of fully synchronized repeat-pass acquisitions, and 0.5, in the case of completely nonsynchronized ones.

In the absence of bursts synchronization, the interferograms computed by using TOPSAR data can be affected by two different effects: interferometric coherence degradation and the possible presence of totally incoherent azimuth stripes. In the following two subsections, we show how these effects can be quantified in terms of the synchronization index in (2).

A. Interferometric Coherence Reduction

This effect is due to the Doppler shift between matching bursts that are not aligned as in the synchronized TOPSAR case [2]. To better analyze this effect, let us consider $f_{\mathrm{DC},p}^{\mathrm{ref}}$ and $f_{\mathrm{DC},p}^{\mathrm{sec}}$ [Hz], which are the DCs relevant to p in the reference and secondary images, respectively, and $\Delta f_{\mathrm{DC},p}$ be the corresponding Doppler separation

$$\Delta f_{\mathrm{DC},p} = |f_{\mathrm{DC},p}^{\mathrm{ref}} - f_{\mathrm{DC},p}^{\mathrm{sec}}|. \tag{3}$$

The condition to be fulfilled to avoid complete spectral separation between the two matching bursts is

$$\Delta f_{\mathrm{DC},p} < B_{\mathrm{az}} \tag{4}$$

wherein B_{az} is the system Doppler bandwidth [Hz] [3]. It can be easily shown that the synchronization index Δx_p in (2) is related to the spectral separation $\Delta f_{\mathrm{DC},p}$ in (3) as follows:

$$\Delta x_p = \frac{\Delta f_{\mathrm{DC},p}}{T k_{t,p}} \tag{5}$$

where $k_{t,p}$ is the DC rate [Hz/s] relevant to p in the considered acquisition burst mode [8], [12]. According to (5), the condition in (4) can be translated into the following restriction in terms of synchronization index

$$\Delta x_p < \frac{B_{\mathrm{az}}}{T k_{t,p}} = \Delta x_{p,\mathrm{critical}} = \frac{\delta x_{p,\mathrm{critical}}}{X}. \tag{6}$$

Note that the critical synchronization index $\Delta x_{p,\mathrm{critical}}$ in (6) represents the maximum allowed value of the synchronization index that guarantees the spectral overlap between two matching bursts. It is noted that in the TOPS mode, $k_{t,p} > (N_S B_{\mathrm{az}}/T)$ [2], thus leading to the following weak upper bound for the critical synchronization index:

$$\Delta x_{p,\mathrm{critical}} < \frac{1}{N_S} \leq \frac{1}{3} \tag{7}$$

where the last inequality comes from the consideration that the existing SAR systems based on TOPS mode exploit a number N_S of subswaths at least equal to 3. From (7), it turns out that the critical synchronization index is well smaller than the limit 0.5 that marks the condition of completely nonsynchronized bursts. This means that within a generic dataset of nonsynchronized repeat-pass TOPS data, enforcement of condition (6) is not guaranteed: checking over this condition is thus mandatory to avoid the exploitation of data pairs useless for interferometric purposes.

As well known, the decorrelation introduced by the spectral separation $\Delta f_{\mathrm{DC},p}$ in (3) can be expressed in terms of interferometric coherence [1], say $\gamma_{\mathrm{DC},p}$ as

$$|\gamma_{\mathrm{DC,p}}| = \left(1 - \frac{\Delta f_{\mathrm{DC},p}}{B_{\mathrm{az}}}\right)\mathrm{rect}\left[\frac{\Delta f_{\mathrm{DC},p} - B_{\mathrm{az}}/2}{B_{\mathrm{az}}}\right] \tag{8}$$

wherein rect[·] is the rectangular pulse function. Using (5) and (6) in (8) leads to the following expression of the interferometric coherence in terms of synchronization index:

$$|\gamma_{\mathrm{dc,p}}| = \left(1 - \frac{\Delta x_p}{\Delta x_{p,\mathrm{critical}}}\right)\mathrm{rect}\left[\frac{\Delta x_p - \Delta x_{p,\mathrm{critical}}/2}{\Delta x_{p,\mathrm{critical}}}\right]. \tag{9}$$

B. Decorrelation Stripes

Due to the Doppler frequency differences between the reference and secondary interfering bursts, in addition to the coherence degradation effect in (9), another effect corrupts the TOPS interferograms in the case of nonsynchronized acquisitions. Specifically, totally noncoherent azimuth stripes will unavoidably appear in the interferograms. To better clarify this aspect, let us refer to Fig. 1, where [Fig. 1(a)] we have highlighted in red the overlapping areas between the adjacent bursts of the same acquisition. As can be seen in the figure, when generating the interferogram, the pixels [orange stripes in Fig. 1(a)] located at the end of the reference bursts (higher Doppler frequencies) interfere with those located at the beginning of the secondary bursts (lower Doppler frequencies). In correspondence to these pixels, the interferogram will be
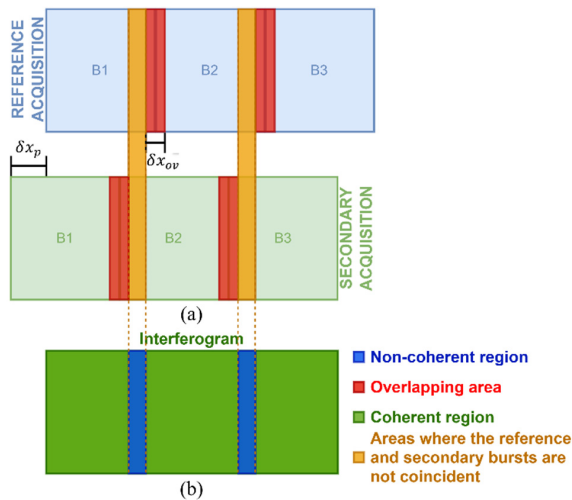
Fig. 1. (a) Sketch of a co-registered pair of images composed by three bursts. For each acquisition, the overlapping area between adjacent bursts is depicted in red. For each couple of interferometric matching bursts, orange stripes are characterized by a Doppler frequency difference greater than the Doppler bandwidth, due to the azimuth shift between acquisitions. (b) Sketch of the corresponding interferogram. Noncoherent stripes (depicted in blue in correspondence to the orange stripes) appear after the interferogram formation because of the Doppler frequency difference.

Fig. 2. Selected interferograms: 4, 8, and 14 fulfill the condition (10), whereas in cases 21, 42, and 43, it is not satisfied.

totally noncoherent [blue stripes in Fig. 1(b)] since the corresponding frequency difference does not fulfill condition (4). In normalized notation, the condition to fulfill to avoid the appearance of these noncoherent stripes is

$$\Delta x_p < \Delta x_{\text{ov}} = \frac{\delta x_{\text{ov}}}{X} = (\alpha - 1) \quad (10)$$

wherein δx_{ov} is the number of overlapping azimuth lines between adjacent bursts of the same acquisition. The normalized azimuth width of the noncoherent stripes is

$$\text{ASW} = \max(\Delta x_p) - \Delta x_{\text{ov}} = \frac{1}{T} \max\left(\frac{\Delta f_{\text{DC},p}}{k_{t,p}}\right) - \alpha + 1 \quad (11)$$

which holds when condition (10) is not satisfied.

It is worth underlining that increasing the overlap between adjacent bursts of the same acquisition may allow avoiding the presence of these noncoherent azimuth stripes. Specifically, if $\Delta x_{\text{ov}} > \max(\Delta x_{p,\text{critical}})$, see (10), as it happens for instance for burst mode systems that exploit at least a two-look configuration [13], this effect is overcome.

This effect has also an important processing consequence. Indeed, TOPSAR interferograms usually present phase discontinuities between bursts. These residual phase jumps can be due to orbital inaccuracies, timing errors, or ionospheric relative azimuth shifts and are corrected by using the enhanced spectral diversity (ESD) algorithm [8], [11]. As the algorithm estimates residual shifts from the spectral separation between the overlapping areas of adjacent bursts of the considered acquisitions, if those overlapping areas are noncoherent, which is the case of the blue stripes in Fig. 1, the ESD algorithm cannot be used.

III. MATERIALS AND STUDY CASE

The test site is located in the southwest of Argentina. It was selected due to the relatively large amount of available
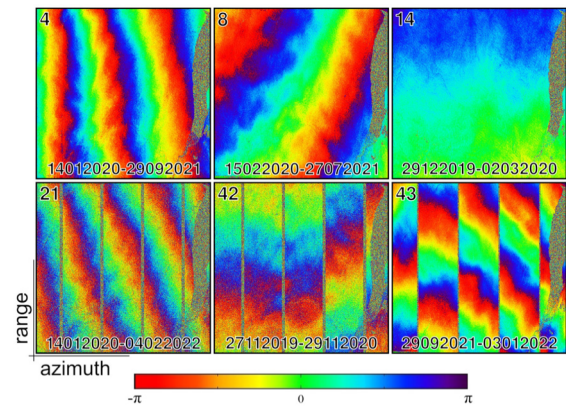
SAOCOM-1 TOPSAR data, acquired in TNB and dual-pol mode. We show the results related to the subswath 5 (S5DP).

The SAR dataset consists of 18 ascending images acquired between 27 December 2019 and 4 February 2022. Each image is composed by a varying number of bursts from 12 to 14, where the common area of the whole dataset comprises only five bursts.

It is observed that computing the interferograms from non-synchronized TOPSAR data mainly follows the same steps already presented in the literature for processing synchronized TOPSAR interferometric pairs. However, some care must be taken in the selection of matching bursts and interburst phase shift removal. These implementation details, not being the focus of this work, are addressed in Appendixes I and II.

We processed scene pairs whose perpendicular baseline is not greater than 2000 m, that is, less than a third of the critical baseline [1] for the system parameters and near the orbital tube of 2500 m for the processed dataset. Furthermore, we allowed DC difference smaller than the system Doppler bandwidth in order to test the limits of this nonsynchronized TOPS system (i.e., 202 Hz [3]).

According to (6) and (10), the synchronization index between the pairs to be considered must be less than ~ 0.15 to obtain Doppler spectrum overlap and less than ~ 0.07 to avoid interburst noncoherent stripes.

By doing so, we computed a total of 48 interferograms, whose properties are summarized in Table I. In 24 of them (50%), the condition in (10) is fulfilled resulting in coherent interferograms without noncoherent stripes. The top row in Fig. 2 shows three selected cases (highlighted in bold in Table I), where good coherence can be appreciated.

In the remaining 24 interferograms, the condition in (10) is not satisfied, resulting in the scenario shown in Fig. 1. Three representative cases (highlighted in bold in Table I) are shown in the bottom row of Fig. 2. Note the noncoherent stripes aligned with the bursts' transitions, particularly noticeable in interferograms 21 and 42. Note also the good coherence in these interferograms, although the Doppler separation between matching bursts (150.5 and 145.7 Hz) is close to the system Doppler bandwidth (202 Hz).

In some cases, i.e., interferograms 18, 24, 25, 31, 32, 34, 47, and 48, decorrelation linked to $\Delta f_{\text{DC},p}$ alone produces a lower coherence than the actually observed (see the last column in

TABLE I
LIST OF THE 48 INTERFEROGRAMS COMPUTED

Id	Reference-Secondary [Day-Month-Year]	$\Delta B_\perp$ [m]	ΔB_{temp} [days]	$\Delta f_{DC,p}$ [Hz]	$\|\gamma_{DC,p}\|$	Δx_p	ASW	Coherence $\bar{x} \pm \sigma$
1	02032020-21052020	1792	80	10.4	0.948	0.008	-	0.58±0.14
2	02032020-22062020	-63	112	6.0	0.970	0.004	-	0.75±0.16
3	02032020-27072021	-393	512	28.4	0.859	0.021	-	0.54±0.15
4	**14012020-29092021**	**-1183**	**624**	**8.7**	**0.957**	**0.006**	**-**	**0.53±0.15**
5	15022020-02032020	-312	16	6.9	0.966	0.005	-	0.79±0.16
6	15022020-21052020	1479	96	3.5	0.983	0.003	-	0.62±0.15
7	15022020-22062020	-376	128	0.9	0.995	0.001	-	0.75±0.17
8	**15022020-27072021**	**-706**	**528**	**35.4**	**0.825**	**0.026**	**-**	**0.50±0.14**
9	21052020-22062020	-1855	32	4.4	0.978	0.003	-	0.63±0.15
10	22062020-27072021	-329	400	34.4	0.830	0.026	-	0.54±0.15
11	24072020-03012022	-58	528	4.0	0.980	0.003	-	0.42±0.16
12	27112019-14012020	156	48	13.7	0.932	0.010	-	0.70±0.16
13	27112019-29092021	-1026	672	22.4	0.889	0.017	-	0.52±0.15
14	**29122019-02032020**	**-1309**	**64**	**18.6**	**0.908**	**0.014**	**-**	**0.69±0.16**
15	29122019-15022020	-996	48	11.6	0.942	0.009	-	0.71±0.16
16	29122019-21052020	482	144	8.1	0.960	0.006	-	0.67±0.16
17	29122019-22062020	-1373	176	12.6	0.938	0.009	-	0.62±0.15
18	02032020-28102020	1804	240	172.2	0.148	0.129	0.058	0.16±0.08
19	03012022-04022022	-401	32	45.4	0.775	0.034	-	0.63±0.15
20	14012020-03012022	-1560	720	105.1	0.480	0.078	0.008	0.28±0.11
21	**14012020-04022022**	**-1961**	**752**	**150.5**	**0.255**	**0.112**	**0.042**	**0.18±0.09**
22	14012020-24072020	-1501	192	101.0	0.500	0.075	0.005	0.26±0.11
23	14012020-29112020	-410	320	159.4	0.211	0.119	0.049	0.17±0.09
24	15022020-28102020	1491	256	179.1	0.113	0.134	0.063	0.16±0.08
25	15022020-29112020	826	288	194.3	0.038	0.145	0.075	0.15±0.08
26	15122020-03012022	714	384	126.2	0.375	0.094	0.024	0.26±0.11
27	15122020-04022022	313	416	80.8	0.600	0.060	-	0.41±0.14
28	15122020-16012021	1695	32	166.1	0.178	0.124	0.054	0.16±0.08
29	16012021-25062021	-1484	160	74.6	0.630	0.056	-	0.43±0.13
30	16012021-28082021	-476	224	164.3	0.178	0.124	0.054	0.17±0.08
31	21052020-28102020	12	160	182.6	0.096	0.136	0.066	0.15±0.08
32	21052020-29112020	-653	192	190.8	0.055	0.143	0.072	0.15±0.08
33	22062020-28102020	1868	128	178.2	0.118	0.133	0.063	0.16±0.08
34	22062020-29112020	1202	160	195.2	0.034	0.146	0.075	0.15±0.08
35	24072020-04022022	-459	560	49.5	0.755	0.037	-	0.34±0.14
36	24072020-15122020	-773	144	130.3	0.355	0.097	0.027	0.19±0.09
37	24072020-29092021	318	432	92.3	0.543	0.069	-	0.26±0.12
38	25062021-28082021	1007	64	89.7	0.547	0.068	-	0.39±0.13
39	27112019-03012022	-1403	768	118.7	0.412	0.089	0.018	0.25±0.11
40	27112019-04022022	-1804	800	164.1	0.187	0.122	0.052	0.17±0.08
41	27112019-24072020	-1344	240	114.7	0.432	0.086	0.015	0.22±0.10
42	**27112019-29112020**	**-254**	**368**	**145.7**	**0.279**	**0.109**	**0.039**	**0.21±0.10**
43	**29092021-03012022**	**-376**	**96**	**96.4**	**0.523**	**0.072**	**0.002**	**0.41±0.13**
44	29092021-04022022	-777	128	141.8	0.298	0.106	0.035	0.25±0.11
45	29112020-29092021	-772	304	168.1	0.168	0.125	0.055	0.17±0.09
46	29122019-27072021	-1702	576	47.0	0.767	0.035	-	0.41±0.13
47	29122019-28102020	495	304	190.8	0.056	0.143	0.072	0.15±0.08
48	29122019-29112020	-170	336	182.7	0.096	0.136	0.066	0.15±0.08

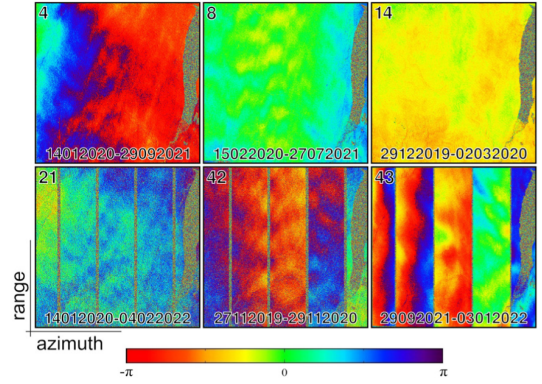|		
$\Delta B_\perp$: perpendicular baseline separation.	$prf = 282.38\ Hz$	$\Delta x_{p,critical} \approx 0.15$
$B_{\perp critical} \approx 10600\ m$	$T = 2.72\ s$	$\alpha \approx 1.07$
ΔB_{temp}: temporal baseline separation.	$X = 768$	$B_{az} \approx 202\ Hz$

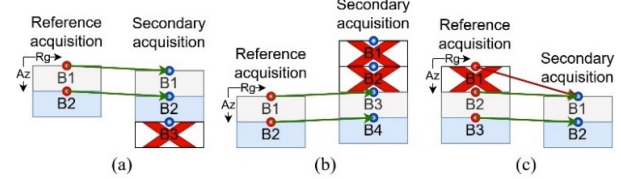Fig. 3. Interferograms of Fig. 2 with the orbital correction applied.

Fig. 4. Relevant to nonsynchronized TOPSAR data. Reference and secondary acquisitions consist of a number of bursts labeled with B1 and B2 ∼BN identifiers. Matching bursts are colored alike. Bursts highlighted with red crosses have no correspondence in the other acquisition. Green arrows highlight the minimum Euclidean distance between the reference and the secondary bursts. (a) Reference bursts are directly aligned with secondary bursts. (b) and (c) Reference bursts are not directly aligned with secondary bursts.

IV. CONCLUSION

This work demonstrates that it is possible to systematically obtain coherent interferograms from SAOCOM-1 data acquired in TOPSAR modes, although bursts synchronization has not been foreseen for these SAOCOM-1 modes.

Out of a time series of 18 acquisitions, we were able to compute 48 interferograms that compose a well-connected interferometric dataset, as can be seen by analyzing Table I, with the potential of being useful for computing deformation time series.

The main open issue is that many interferograms present phase biases that cannot be corrected using the ESD algorithm due to SAOCOM-1 lack of synchronization and noncoherent stripes, which cannot be straightforwardly removed. An approach to address this problem, which is a matter of current study and future work, is to take benefit from the overlapping area between consecutive subswaths for estimating the phase offsets between adjacent bursts.

Finally, we remark that the proposed approach has been applied to a single subswath (S5DP). However, it is highlighted that the same procedure is applicable to the other subswaths (S6DP and S7DP) that compose the acquisitions, given that the Doppler bandwidth (∼212 and ∼225 Hz) is even wider than that considered in our test case (∼202 Hz).

APPENDIX A

In this appendix, we clarify how to select matching bursts in nonsynchronized TOPS datasets.

The lack of synchronization in SAOCOM-1 TOPSAR data implies that there is not a common time frame for bursts acquired in repeat-pass acquisitions, which is useful for recognizing corresponding bursts [8]. Therefore, bursts of different acquisitions do not always cover the same ground area.

Table I). This can be attributed to the used coherence estimator, which overestimates the values when coherence is low [14].

Despite the good results in terms of coherence, there are phase artifacts affecting many interferograms. In particular, there are residual phase ramps that can be related to errors in the orbital ephemerides, which is a known issue [5], and ionospheric effects that can produce azimuthal phase ramps indistinguishable from those derived from orbital uncertainty [15], [16]. This kind of artifact, assuming a purely orbital cause, can be dealt with by using the approach proposed in [17], which estimates and applies orbital corrections before the interferogram formation. We applied it to our dataset, resulting in the corrected interferograms shown in Fig. 3. Notice that the orbital correction is also applicable to the interferograms with interburst phase discontinuities. In these cases, orbital corrections are computed by considering only a single burst and propagating them to the whole interferogram. Obviously, these phase jumps limit the potential use of the entire interferogram reducing to a single burst the effective area that can be investigated.

For the sake of simplicity, let us consider only two acquisitions. Two scenarios are possible: the reference bursts can be directly aligned with the secondary bursts [see Fig. 4(a)] or not [see Fig. 4(b) and (c)]. To deal with both scenarios, a common burst reference frame must be defined. To this aim, we identify the middle range point of the first line (azimuth time), in both images and for each burst, and we translate these tie points into a geocentric Cartesian system using the orbital information. Then, we compute the Euclidean distance from each tie point of the reference bursts to all the tie points of the secondary bursts: the pair with the lowest distance will present the largest azimuth spectral overlap, thus defining the searched burst matching.

Note that to correctly address the possibility that a generic burst is not present in one of the two acquisitions, this distance should be computed by considering the tie points of all the reference and secondary bursts. To better clarify this aspect, let us refer to the example of Fig. 4(c). In this case, if for the reference acquisition, we used only the tie point of B1, we would match this burst B1 and the secondary burst B1 (red arrow). This, however, would be not correct since, actually, the reference burst B2 matches the secondary burst B1 (green arrow).

APPENDIX B

In this appendix, we briefly summarize the rationale of the ESD algorithm in [8] and describe how we implement it.

The interburst phase discontinuities are usually compensated by using the ESD algorithm proposed in [8]. It exploits the spectral separation between the overlapping areas of adjacent bursts in the considered acquisitions for estimating residual geometrical shifts. The formulation in [8] assumes that the estimated phase offset is essentially the same in all consecutive bursts. Thus, the residual shift is estimated as the average ratio between the phase offset and the Doppler frequency differences at all the pixels in the superposition areas [8]

$$\hat{\Delta y} = \frac{\mathrm{prf}}{2\pi} \cdot \frac{\arg\{\langle e^{j\varphi_{\mathrm{ESD},p}}\rangle\}}{\langle \Delta f_{\mathrm{DC},p}^{\mathrm{ovl}} \rangle} \quad (12)$$

wherein $\langle \cdot \rangle$ indicates the average value, $\hat{\Delta y}$ is an approximation for the estimation of the residual shift, $\varphi_{\mathrm{ESD},p}$ is the phase offset at pixel p, and $\Delta f_{\mathrm{DC},p}^{\mathrm{ovl}}$ stands for the DC frequency difference in the overlap area for each burst.

We introduced a slight modification for accounting for nonstationary cases where nonrigid corrections need to be used [8], such as interferograms affected by strong azimuth gradients introduced by the ionosphere [15]. We estimated one phase offset value per burst transition and used them to compute the following cumulative interferometric phase function:

$$\begin{cases} \varphi_b = 0 & \text{if } b = 0 \\ \varphi_b = \sum_{i=0}^{b-1} \varphi_{\mathrm{ESD}_i} & \text{if } b > 0 \end{cases} \quad (13)$$

which we directly apply to the interferogram as an additional phase correction. In (13), b is the burst number, the index i identifies the interchannel overlapping areas, and φ_{ESD_i} is the mean phase difference in the ith interchannel overlapping area computed as in [8].

REFERENCES

[1] G. Franceschetti and R. Lanari, *Synthetic Aperture Radar Processing*. Boca Raton, FL, USA: CRC Press, 1999, doi: 10.1201/9780203737484.

[2] F. De Zan and A. M. Guarnieri, "TOPSAR: Terrain observation by progressive scans," *IEEE Trans. Geosci. Remote Sens.*, vol. 44, no. 9, pp. 2352–2360, Sep. 2006, doi: 10.1109/TGRS.2006.873853.

[3] CONAE. (2020). *Catálogo SAOCOM, SAOCOM-1 Level 1 Products Format*. [Online]. Available: https://catalogos.conae.gov.ar/catalogo/docs/SAOCOM/SAOCOM-1_SAR_Level-1_Product-Format_13Jan2020.pdf

[4] CONAE. (2019). *Misiones Satelitales*. [Online]. Available: https://www.argentina.gob.ar/ciencia/conae/misiones-espaciales/saocom

[5] Y. Roa et al., "First assessment of the interferometric capabilities of SAOCOM-1A: New results over the domuyo volcano, Neuquén Argentina," *J. South Amer. Earth Sci.*, vol. 106, Mar. 2021, Art. no. 102882.

[6] M. Camejo-Harry et al., "Monitoring volcano deformation at La Soufrière, St. Vincent during the 2020-21 eruption with insights into its magma plumbing system architecture," *Geol. Soc., London, Special Publications*, vol. 539, no. 1, Apr. 2024, Art. no. SP539-2022270, doi: 10.1144/SP539-2022-270.

[7] C. De Luca et al., "On the first results of the DInSAR-3M project: A focus on the interferometric exploitation of saocom SAR images," in *Proc. IEEE Int. Geosci. Remote Sens. Symp. (IGARSS)*, Kuala Lumpur, Malaysia, Jul. 2022, pp. 4502–4505, doi: 10.1109/IGARSS46834.2022.9884715.

[8] N. Yagüe-Martínez et al., "Interferometric processing of Sentinel-1 TOPS data," *IEEE Trans. Geosci. Remote Sens.*, vol. 54, no. 4, pp. 2220–2234, Apr. 2016, doi: 10.1109/TGRS.2015.2497902.

[9] P. Prats-Iraola, R. Scheiber, L. Marotti, S. Wollstadt, and A. Reigber, "TOPS interferometry with TerraSAR-X," *IEEE Trans. Geosci. Remote Sens.*, vol. 50, no. 8, pp. 3179–3188, Aug. 2012, doi: 10.1109/TGRS.2011.2178247.

[10] E. Sansosti, P. Berardino, M. Manunta, F. Serafino, and G. Fornaro, "Geometrical SAR image registration," *IEEE Trans. Geosci. Remote Sens.*, vol. 44, no. 10, pp. 2861–2870, Oct. 2006, doi: 10.1109/TGRS.2006.875787.

[11] R. Scheiber and A. Moreira, "Coregistration of interferometric SAR images using spectral diversity," *IEEE Trans. Geosci. Remote Sens.*, vol. 38, no. 5, pp. 2179–2191, Sep. 2000, doi: 10.1109/36.868876.

[12] N. Miranda, "Definition of the TOPS SLC deramping function for products generated by the S-1 IPF," Eur. Space Agency, Tech. Rep. COPE-GSEG-EOPG-TN-14-0025, Jan. 2017.

[13] S. Perna, F. Longo, S. Zoffoli, M. Davidson, L. Iannini, and R. Lanari, "A conceptual performance study on a two-look ScanSAR mode configuration for the forthcoming ROSE-L mission," *IEEE Trans. Geosci. Remote Sens.*, p. 11, Dec. 2023, doi: 10.1109/TGRS.2023.3344537.

[14] R. Touzi, A. Lopes, J. Bruniquel, and P. W. Vachon, "Coherence estimation for SAR imagery," *IEEE Trans. Geosci. Remote Sens.*, vol. 37, no. 1, pp. 135–149, Jan. 1999, doi: 10.1109/36.739146.

[15] G. Gomba, F. R. González, and F. De Zan, "Ionospheric phase screen compensation for the Sentinel-1 TOPS and ALOS-2 ScanSAR modes," *IEEE Trans. Geosci. Remote Sens.*, vol. 55, no. 1, pp. 223–235, Jan. 2017, doi: 10.1109/TGRS.2016.2604461.

[16] C. Liang, P. Agram, M. Simons, and E. J. Fielding, "Ionospheric correction of InSAR time series analysis of C-band Sentinel-1 TOPS data," *IEEE Trans. Geosci. Remote Sens.*, vol. 57, no. 9, pp. 6755–6773, Sep. 2019, doi: 10.1109/TGRS.2019.2908494.

[17] A. Pepe, P. Berardino, M. Bonano, L. D. Euillades, R. Lanari, and E. Sansosti, "SBAS-based satellite orbit correction for the generation of DInSAR time-series: Application to RADARSAT-1 data," *IEEE Trans. Geosci. Remote Sens.*, vol. 49, no. 12, pp. 5150–5165, Dec. 2011, doi: 10.1109/TGRS.2011.2155069.